particles

IMPACT FACTOR 1.7

CITESCORE 3.2

Article

Thermal Conductivity and Thermal Hall Effect in Dense Electron-Ion Plasma

Arus Harutyunyan and Armen Sedrakian

Special Issue

Selected Papers from "The Modern Physics of Compact Stars and Relativistic Gravity 2023"

Edited by

Prof. Dr. Aram Saharian

MDPI

https://doi.org/10.3390/particles7040059

particles

MDPI

Article

Thermal Conductivity and Thermal Hall Effect in Dense Electron-Ion Plasma

Arus Harutyunyan [1,2,*,†] and Armen Sedrakian [3,4,†]

[1] Byurakan Astrophysical Observatory, Byurakan 0213, Armenia
[2] Department of Physics, Yerevan State University, Yerevan 0025, Armenia
[3] Frankfurt Institute for Advanced Studies, D-60438 Frankfurt am Main, Germany; sedrakian@fias.uni-frankfurt.de
[4] Institute of Theoretical Physics, University of Wrocław, 50-204 Wrocław, Poland
* Correspondence: arus@bao.sci.am
† These authors contributed equally to this work.

Abstract: In this study, we examine thermal conductivity and the thermal Hall effect in electron-ion plasmas relevant to hot neutron stars, white dwarfs, and binary neutron star mergers, focusing on densities found in the outer crusts of neutron stars and the interiors of white dwarfs. We consider plasma consisting of single species of ions, which could be either iron ^{56}Fe or carbon ^{12}C nuclei. The temperature range explored is from the melting temperature of the solid $T \sim 10^9$ K up to 10^{11} K. This covers both degenerate and non-degenerate electron regimes. We find that thermal conductivity increases with density and temperature for which we provide analytical scaling relations valid in different regimes. The impact of magnetic fields on thermal conductivity is also analyzed, showing anisotropy in low-density regions and the presence of the thermal Hall effect characterized by the Righi–Leduc coefficient. The transition froma degenerate to non-degenerate regime is characterized by a minimum ratio of thermal conductivity to temperature, which is analogous to the minimum observed already in the case of electrical conductivity. We provide also formulas fit to our numerical results, which can be used in dissipative magneto-hydrodynamics simulations of warm compact stars.

Keywords: neutron stars; transport phenomena; Boltzmann theory

Citation: Harutyunyan, A.; Sedrakian, A. Thermal Conductivity and Thermal Hall Effect in Dense Electron-Ion Plasma. *Particles* **2024**, *7*, 967–983. https://doi.org/10.3390/particles7040059

Academic Editor: Nicolas Chamel

Received: 3 September 2024
Revised: 3 November 2024
Accepted: 7 November 2024
Published: 11 November 2024

1. Introduction

In the outer and inner crust of neutron stars and the cores of white dwarfs, the plasma is composed primarily of degenerate electrons and various ion species, depending on the density and temperature. These ions might include light nuclei (like hydrogen and helium) and heavier nuclei (iron), with possible other exotic nuclei deeper within the crust of a neutron star. In mature cold compact stars, the electrons are highly degenerate, i.e., they fill a Fermi sphere. The transport coefficients of such plasmas, including thermal conductivity, in the liquid and solid phases, have been the focus of research for many decades [1–12]. More recently, the transport in high-temperature, semi- or non-degenerate regimes has become of great interest, mainly in the context of binary neutron star mergers, but also proto-neutron stars born in supernova explosions, which contain electron-ion plasma that can be non-degenerate due to high temperatures. Understanding transport in such an environment is needed for setting up dissipative relativistic hydrodynamics, which ultimately determines the large-scale behavior of these objects and allows us to model them numerically. Early studies concentrated on electrical conductivity [13,14] and bulk viscosity [15–18]. However, the simultaneous presence of magnetic and electric fields and compositional and thermal gradients couples the various transport channels. This motivates our investigation of thermal conductivity effects within the same framework for electrical conductivity.

Neutron stars commonly have extremely strong magnetic fields, ranging from canonical 10^{12} G to magnetar-strength $\geq 10^{15}$ G fields. Such strong fields drastically alter the behavior of charged particles in their crusts. The magnetic field can cause anisotropies in thermal and electrical conductivities as, for example, heat flows more efficiently along magnetic field lines than across them. Additionally, they lead to the Hall effect, where the motion of electrons under the influence of a magnetic field generates transverse electric fields and/or temperature gradients. Furthermore, the early stages of hot proto-neutron stars and post-merger remnants may feature large thermal gradients driven by violent fluid dynamics. The simultaneous presence of large magnetic fields and thermal gradients can then lead to complex feedback loops between the temperature and magnetic field evolution of such objects. Models were put forward early on to describe the generation of strong fields via the dynamo effect driven by strong thermal gradients, i.e., where the heat flux drives the circulation that amplifies the magnetic field; this type of model is known as thermoelectric [19–23]. Another class of models concerns the thermo-magnetic evolution of compact stars where their cooling is strongly affected by the presence of strong magnetic fields, their decay, and internal heating [24–27]. The third class of models describes neutron star binary mergers in the presence of strong magnetic fields within resistive magneto-hydrodynamics. Estimates of efficiency of the conductivity and Hall effect in this context show the necessity of resistive studies of mergers for proper understanding of the spectrum of emitted gravitational waves [28].

In this work, we compute the thermal conductivity tensor as well as the Righi–Leduc coefficient describing the thermal Hall effect in the magnetized outer crust of a warm neutron star. In this domain of the crust, the electrons are the main charge and heat carriers, and the transport coefficients are dominated by the electron scattering off the ions. The formalism we use here was previously developed for assessment of electrical conductivity of electron-ion plasma [13,14,29]. Before proceeding, let us point out that the thermal conductivity was computed in the cold regime, including the case where ions solidify in the context of cold neutron stars in Refs. [1,2,4,6,8,11,30,31] (see [12] for a review). Work on the conductive opacity of low- and intermediate-mass stars has also been carried out [32,33] within formalism applicable at arbitrary temperatures, densities, and magnetic fields. Their numerical work is focused on lower densities ($\rho \leq 10^8$ g cm^3), temperatures ($T \leq 10^8$ K), and light element (H and He) composition.

This paper is organized as follows. Section 2 discusses the phase diagram of one-component plasma in the regimes of interest for neutron stars and white dwarfs. In Section 3, we present the computation energy-dependent relaxation time starting from the Boltzmann equation and the key approximations that underlie our formalism. In Section 4, we derive the tensors of the thermal conductivity in magnetic fields by evaluating the electric and thermal current when the electric field and temperature gradient are present simultaneously. Section 5 presents the numerical results for the thermal conductivity and the thermal Hall effect in the density, temperature, and B-field regimes of interest. Our results are summarized in Section 6.

We use the natural (Gaussian) units with $\hbar = c = k_B = k_e = 1$, $e = \sqrt{\alpha}$, and $\alpha = 1/137$, and the metric signature $(1, -1, -1, -1)$.

2. Physical Conditions

Matter in the outer crusts of neutron stars and the interiors of white dwarfs consists of fully ionized ions (i.e., atomic nuclei) and almost non-interacting Fermi gas of relativistic electrons, which are the main transporters of charge and heat in the system. Electron (n_e) and ion (n_i)densities are related by the charge local neutrality condition $n_e = Zn_i$, where Z is the ion charge number. The almost free gas of electrons becomes degenerate below the Fermi temperature $T_F = \varepsilon_F - m$, where $\varepsilon_F = (p_F^2 + m^2)^{1/2}$ is the Fermi energy, $p_F = (3\pi^2 n_e)^{1/3}$ is the Fermi momentum, and m is the electron mass. The state of the ionic component is characterized by the so-called Coulomb plasma parameter

$$\Gamma = \frac{T_C}{T}, \quad T_C = \frac{e^2 Z^2}{a_i}, \tag{1}$$

where e is the elementary charge, T is the temperature, and $a_i = (4\pi n_i/3)^{-1/3}$ is the radius of the spherical volume per ion. If $\Gamma \ll 1$, or, equivalently, $T \gg T_C$, ions form weakly coupled Boltzmann gas. In the opposite regime, $\Gamma \geq 1$ ions are strongly coupled and form either a liquid (for $\Gamma \leq \Gamma_m \simeq 160$) or a lattice (for $\Gamma > \Gamma_m$). Correspondingly, the melting temperature of the lattice is defined as $T_m = (Ze)^2/\Gamma_m a_i$. The ion plasma temperature is represented by

$$T_p = \left(\frac{4\pi Z^2 e^2 n_i}{M}\right)^{1/2}, \tag{2}$$

where M is the ion mass, and further separates the regimes of classical ($T \geq T_p$) and quantum ($T \leq T_p$) lattice. In the second case, the quantization of the lattice oscillations becomes important. Figure 1 shows the temperature-density phase diagram of the crustal plasma composed of iron ^{56}Fe and carbon ^{12}C nuclei.

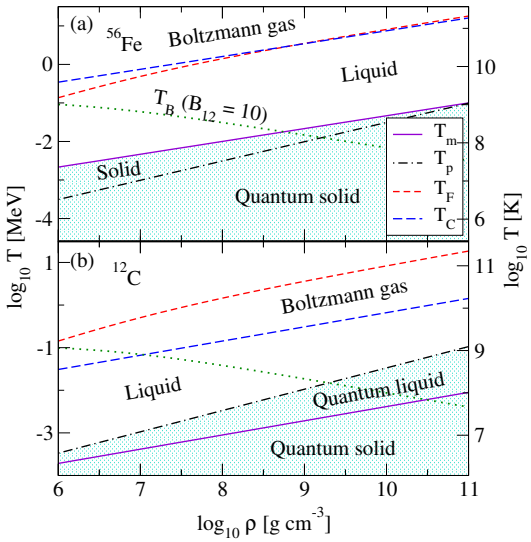

Figure 1. The temperature-density phase diagram of dense plasma composed of iron ^{56}Fe (**a**) and carbon ^{12}C (**b**). The electron gas degeneracy sets in below the Fermi temperature T_F (short dashed lines). The ionic component solidifies below the melting temperature T_m (solid lines), while quantum effects become important below the plasma temperature (dash-dotted lines). For temperatures above T_C (long dashed lines), the ionic component forms a Boltzmann gas. Note that for ^{12}C, quantum effects become important in the portion of the phase diagram lying between the lines $T_p(\rho)$ and $T_m(\rho)$. In addition, the dotted lines show the temperature T_B below which the quantization of the electron energy in the magnetic field becomes important for $B_{12} = 10$. The present study does not cover the shaded portion of the phase diagram.

The general structure of the phase diagram is similar for ^{56}Fe and carbon ^{12}C nulcei. However, an important difference appears in the low-temperature regime: while the plasma temperature is always smaller than the melting temperature in the case of ^{56}Fe, in the case of ^{12}C instead, the quantum effects become important before the solidification sets in. In addition, the phase diagrams for these elements do not take into account that at high temperatures and/or densities, the energy and pressure are sufficient to overcome the Coulomb barrier, allowing nuclei to fuse almost instantaneously. This fusion process occurs more rapidly than the rates at which the plasma can maintain its low-Z composition. As a result, rather than remaining in a stable plasma state, the particles in the plasma will quickly undergo fusion reactions, leading to the formation of heavier elements. Consequently, the existence of a low-Z plasma becomes untenable in such environments.

We note also that the phase diagram shown in Figure 1 is applicable to the non-magnetized crust. In the presence of magnetic fields, the Fermi temperature of electrons is modified at low densities where the Landau quantization is important. This is the case at temperatures $T \leq T_B$, with

$$T_B = \frac{eB}{\varepsilon_F}, \tag{3}$$

which is the characteristic temperature which separates the quantized and non-quantized regimes of the phase diagram [10]. The temperature T_B is shown in Figure 1, with dotted lines for the magnetic field $B_{12} = 10$. As seen from the figure, for $B_{12} \leq 10$, the Landau quantization can be neglected at temperatures $T \geq 0.1$ MeV, which is the main regime of our interest. However, for higher magnetic fields, the quantization of electron energies becomes important in the low density domain of the phase diagram. In this work, we will restrict our analysis to the non-quantizing regime, keeping in mind that the extrapolation of the obtained results to higher values of magnetic field should be regarded as the classical average values of the transport coefficients in the regime where the quantization is important.

3. Thermal Conductivity and Thermal Hall Effect from Boltzmann Equation

We start with the Boltzmann equation for the electron distribution function

$$\frac{\partial f}{\partial t} + \boldsymbol{v}\frac{\partial f}{\partial \boldsymbol{r}} - e(\boldsymbol{E} + \boldsymbol{v} \times \boldsymbol{B})\frac{\partial f}{\partial \boldsymbol{p}} = I[f], \tag{4}$$

where $\boldsymbol{E}$ and $\boldsymbol{B}$ are the electric and magnetic fields, $\boldsymbol{v} = \partial\varepsilon/\partial\boldsymbol{p}$ is the electron velocity with $\varepsilon = \sqrt{p^2 + m^2}$ and m being the electron mass, e is the unit charge, and $I[f]$ is the electron-ion collision integral given by

$$I[f] = -(2\pi)^4 \sum_{234} |\mathcal{M}_{12\to34}|^2 \delta^{(4)}(p_1 + p_2 - p_3 - p_4)[f_1(1 - f_3)g_2 - f_3(1 - f_1)g_4], \tag{5}$$

where $f_{1,3} = f(p_{1,3})$ are the electrons' and $g_{2,4} = g(p_{2,4})$ are the ions' distribution functions, $\mathcal{M}_{12\to34}$ is the electron-ion scattering matrix element, and $\sum_i = \int d\boldsymbol{p}_i/(2\pi)^3$. We will refer the study of thermal conductivity resulting from electron–electron collisions to a future work, as its contribution is minor to the nuclear charge numbers considered here, see also [31–33].

As ions form a classical fluid in equilibrium, the function $g(p)$ is given by the Maxwell–Boltzmann distribution

$$g(p) = n_i \left(\frac{2\pi}{MT}\right)^{3/2} \exp\left(-\frac{p^2}{2MT}\right). \tag{6}$$

To linearize the kinetic equation, the electron distribution function can be written in the form

$$f = f^0 + \delta f, \quad \delta f = -\phi\frac{\partial f^0}{\partial \varepsilon}. \tag{7}$$

where

$$f^0(\varepsilon) = \frac{1}{e^{\beta(\varepsilon-\mu)} + 1} \tag{8}$$

is the local Fermi distribution function with $\beta = T^{-1}$, μ is the electron chemical potential, and $\delta f \ll f^0$ is a small perturbation. To derive the thermal conductivity, we assume that the temperature T and the electron chemical potential μ are slowly varying functions of space: $T = T(\boldsymbol{x})$, $\mu = \mu(\boldsymbol{x})$. Using Equation (8), the space and momentum derivatives can be computed in the drift term of Equation (4). Note that in Equation (4), the substitution

$f \to f^0$ can be applied to the terms involving space-time derivatives or the electric field. However, in the term involving the magnetic field, the perturbation must be retained because, in equilibrium, the magnetic field's effect vanishes since $[\boldsymbol{v} \times \boldsymbol{B}](\partial f^0/\partial \boldsymbol{p}) \propto [\boldsymbol{v} \times \boldsymbol{B}]\boldsymbol{v} = 0$. Thus, for the third term in Equation (4), we obtain

$$e(\boldsymbol{E} + \boldsymbol{v} \times \boldsymbol{B})\frac{\partial f}{\partial \boldsymbol{p}} = e\boldsymbol{v} \cdot \boldsymbol{E}\frac{\partial f^0}{\partial \varepsilon} - e[\boldsymbol{v} \times \boldsymbol{B}]\frac{\partial f^0}{\partial \varepsilon}\frac{\partial \phi}{\partial \boldsymbol{p}}. \tag{9}$$

Using the space- and momentum-derivatives of Equations (8) and (9), we obtain the left-hand-side of Equation (4) at linear order in macroscopic gradients

$$\frac{df}{dt} = -\frac{\partial f^0}{\partial \varepsilon}\left(e\boldsymbol{v} \cdot \boldsymbol{F} - e[\boldsymbol{v} \times \boldsymbol{B}]\frac{\partial \phi}{\partial \boldsymbol{p}}\right), \tag{10}$$

where we define

$$\boldsymbol{F} = \boldsymbol{E}' + \frac{\varepsilon - \mu}{eT}\nabla T, \qquad e\boldsymbol{E}' = e\boldsymbol{E} + \nabla \mu. \tag{11}$$

Thus, the linearized Boltzmann equation reads

$$\frac{\partial f^0}{\partial \varepsilon}\left(e\boldsymbol{v} \cdot \boldsymbol{F} - e[\boldsymbol{v} \times \boldsymbol{B}]\frac{\partial \phi}{\partial \boldsymbol{p}}\right) = -I[\phi], \tag{12}$$

with the linearized collision integral given by

$$I[\phi] = -(2\pi)^4 \beta \sum_{234} |\mathcal{M}_{12\to 34}|^2 \delta^{(4)}(p_1 + p_2 - p_3 - p_4) f_1^0 (1 - f_3^0) g_2 (\phi_1 - \phi_3). \tag{13}$$

The solution of Equation (10) can be obtained from Equation (15) of Ref. [13] by substitution $\boldsymbol{E} \to \boldsymbol{F}$

$$\phi = -\frac{e\tau}{1 + (\omega_c \tau)^2} v_i \left(\delta_{ij} - \omega_c \tau \varepsilon_{ijk} b_k + (\omega_c \tau)^2 b_i b_j\right) F_j, \tag{14}$$

where $\boldsymbol{b} = \boldsymbol{B}/B$, $\omega_c = eB/\varepsilon$ is the electron cyclotron frequency, and the relaxation time is defined by

$$\tau^{-1}(\varepsilon_1) = (2\pi)^{-5} \int d\boldsymbol{q} \int d\boldsymbol{p}_2 \, |\mathcal{M}_{12\to 34}|^2 \frac{\boldsymbol{q} \cdot \boldsymbol{p}_1}{p_1^2} \delta(\varepsilon_1 + \varepsilon_2 - \varepsilon_3 - \varepsilon_4) g_2 \frac{1 - f_3^0}{1 - f_1^0}. \tag{15}$$

The matrix element includes several corrections to the bare Coulomb electron-ion interaction. The screening of the interaction is included in terms of the hard-thermal-loop polarization tensor of QED plasma in the low-frequency limit (see Sec. IV D of Ref. [13]). The ion–ion correlations are accounted for by means of the static structure factor $S(q)$ of one-component plasma, and the finite nuclear size is included via the nuclear form factor $F(q)$ (see Ref. [13] and the discussion below). The final expression for the relaxation time reads

$$\begin{aligned} \tau^{-1}(\varepsilon) &= \frac{\pi Z^2 e^4 n_i}{\varepsilon p^3} \sqrt{\frac{M}{2\pi T}} \int_{-\infty}^{\varepsilon - m} d\omega \, e^{-\omega/2T} \frac{f^0(\varepsilon - \omega)}{f^0(\varepsilon)} \int_{q_-}^{q_+} dq \left(q^2 - \omega^2 + 2\varepsilon\omega\right) \\ &\times e^{-\omega^2 M/2q^2 T} e^{-q^2/8MT} S(q) F^2(q) \frac{(2\varepsilon - \omega)^2 - q^2}{|q^2 + \Pi_L|^2}, \end{aligned} \tag{16}$$

where $q_\pm = |\sqrt{p^2 - (2\omega\varepsilon - \omega^2)} \pm p|$, and the real and imaginary parts of the longitudinal polarization are given by $\Pi_L(q, \omega) = q_D^2 \chi_l$, where

$$\mathrm{Re}\chi_l(q, \omega) \simeq 1 - \left(\frac{\omega}{q}\right)^2, \quad \mathrm{Im}\chi_l(q, \omega) \simeq -\frac{\pi\omega}{2q}, \tag{17}$$

where the Debye wave-number q_D at finite temperature is given by

$$q_D^2 = -\frac{4e^2}{\pi}\int_0^\infty dp\, p^2 \frac{\partial f^0}{\partial \varepsilon}. \tag{18}$$

Note that we neglected the transverse part of the scattering in the matrix element as its contribution to the relaxation time is small in the regime of interest of this work (for the full expression, see [13]). Equations (16)–(18) are valid for arbitrary temperatures and across the full spectrum of degeneracies of electrons.

The relaxation time (16) takes a simpler form when the ionic component of the plasma is considered at zero temperature and nuclear recoil is neglected (see Appendix A of [13]):

$$\tau^{-1}(\varepsilon) = \frac{4\pi Z^2 e^4 n_i}{\varepsilon p^3}\int_0^{2p} dq q^3 S(q) F^2(q) \frac{\varepsilon^2 - (q/2)^2}{|q^2 + \Pi_L(0,q)|^2}. \tag{19}$$

The integral in this expression is known as *Coulomb logarithm (CL)* [2,34,35]. It has been widely used in the previous literature to accommodate the influence of correlations on the transport in electron-ion plasma. In this form, it can be applied at arbitrary temperatures, as long as the finite-temperature effects on the ionic component and recoil can be neglected (see [10,32,33]). The many-body approximation enters the CL via the ion structure factor $S(q,\omega)$, which describes the correlations in the ionic component and the longitudinal polarization tensor of the electrons $\Pi_L(\omega,q)$. The state of the art computations of $S(q,\omega)$, typically taken in the static limit $\omega = 0$, are based on hypernetted-chain or Monte Carlo methods for classical one-component plasma. Itoh et al. [5] implemented in their low-temperature thermal conductivity evaluation the results of hypernetted-chain computations of static structure factor for various values of the Γ parameter, and compared their results for the CL to that of Ref. [2] for ^{56}Fe and ^{12}C. They also implemented the low-temperature random-phase-approximation polarization tensor for relativistic electrons in the static ($\omega = 0$) limit given by [36]. The finite-temperature computations of [32,33] for low-mass stars used a fit formula for CL derived in [10], which is informed by fits to hypernetted chain computations of one-component plasma given in [37]. This fit formula also includes screening through its dependence on the Thomas–Fermi and Debye wave-lengths. In our computations, we adopted the same approach as in [13]. Specifically, the static structure factor is taken from the fits to Monte Carlo simulations of a one-component plasma [38–40]. The screening is accounted through hard-thermal-loop QED polarization functions in the low-frequency limit. This formalism does not impose any restrictions on the temperature or degeneracy of the electrons.

4. Electric and Thermal Currents

We proceed now to the computation of the electrical and thermal currents using the expression (11) for $\boldsymbol{F}$. Using the standard kinetic theory definitions we find [41]

$$j_k = \int \frac{2d\boldsymbol{p}}{(2\pi)^3} e v_k \phi \frac{\partial f^0}{\partial \varepsilon} = \sigma_{kj} E'_j - \alpha_{kj}\partial_j T, \tag{20}$$

and

$$q_k = -\int \frac{2d\boldsymbol{p}}{(2\pi)^3} (\varepsilon - \mu) v_k \phi \frac{\partial f^0}{\partial \varepsilon} = \tilde{\alpha}_{kj} E'_j - \tilde{\kappa}_{kj}\partial_j T, \tag{21}$$

where

$$\sigma_{kj} = -\int \frac{2d\boldsymbol{p}}{(2\pi)^3}\frac{\partial f^0}{\partial \varepsilon}\frac{e^2\tau}{1+(\omega_c\tau)^2}v_k v_i\Big[\delta_{ij}-\omega_c\tau\varepsilon_{ijm}b_m+(\omega_c\tau)^2 b_i b_j\Big] \quad (22)$$

$$\alpha_{kj} = -\int \frac{2d\boldsymbol{p}}{(2\pi)^3}\frac{\partial f^0}{\partial \varepsilon}\frac{e(\varepsilon-\mu)\tau}{1+(\omega_c\tau)^2}v_k v_i\Big[\delta_{ij}-\omega_c\tau\varepsilon_{ijm}b_m+(\omega_c\tau)^2 b_i b_j\Big]T^{-1} \quad (23)$$

$$\tilde{\alpha}_{kj} = \int \frac{2d\boldsymbol{p}}{(2\pi)^3}\frac{\partial f^0}{\partial \varepsilon}\frac{e(\varepsilon-\mu)\tau}{1+(\omega_c\tau)^2}v_k v_i\Big[\delta_{ij}-\omega_c\tau\varepsilon_{ijm}b_m+(\omega_c\tau)^2 b_i b_j\Big] \quad (24)$$

$$\tilde{\kappa}_{kj} = -\int \frac{2d\boldsymbol{p}}{(2\pi)^3}\frac{\partial f^0}{\partial \varepsilon}\frac{(\varepsilon-\mu)^2\tau}{1+(\omega_c\tau)^2}v_k v_i\Big[\delta_{ij}-\omega_c\tau\varepsilon_{ijm}b_m+(\omega_c\tau)^2 b_i b_j\Big]T^{-1}. \quad (25)$$

These expressions for transport coefficients are valid for arbitrary temperatures (see [41]). They have been employed earlier in the context of low-temperature neutron stars and in the cases of non-quantizing [3] and quantizing [10,12,42] magnetic fields and finite-temperature low-mass stars [32,33]. Note the simplification in the low-temperature limit, $\partial f^0/\partial\varepsilon \to -\delta(\varepsilon-\varepsilon_F)$, which removes the necessity for numerical integration.

We will next assume without loss of generality that the magnetic field is directed along the z axis. Inverting Equations (20) and (21) we find

$$\boldsymbol{E}' = \hat{\rho}\boldsymbol{j} - \hat{Q}\nabla T, \qquad \boldsymbol{q} = -\hat{\kappa}\nabla T - T\hat{Q}\boldsymbol{j}, \quad (26)$$

where $\hat{\rho} = \hat{\sigma}^{-1}$ and $\hat{\sigma}$ are the matrices of electrical resistivity and conductivity, respectively; $\hat{Q} = -\hat{\rho}\hat{\alpha}$ is the matrix of thermopower; and $\hat{\kappa} = \hat{\tilde{\kappa}} + T\hat{\alpha}\hat{Q}$ is the matrix of thermal conductivity. These matrices of the transport coefficients are given explicitly by

$$\hat{\sigma} = \begin{pmatrix}\sigma_0 & -\sigma_1 & 0\\ \sigma_1 & \sigma_0 & 0\\ 0 & 0 & \sigma\end{pmatrix}, \quad \hat{\alpha} = \begin{pmatrix}\alpha_0 & -\alpha_1 & 0\\ \alpha_1 & \alpha_0 & 0\\ 0 & 0 & \alpha\end{pmatrix},$$
$$\hat{\tilde{\kappa}} = \begin{pmatrix}\tilde{\kappa}_0 & -\tilde{\kappa}_1 & 0\\ \tilde{\kappa}_1 & \tilde{\kappa}_0 & 0\\ 0 & 0 & \tilde{\kappa}\end{pmatrix}, \quad \hat{\tilde{Q}} = \begin{pmatrix}Q_0 & -Q_1 & 0\\ Q_1 & Q_0 & 0\\ 0 & 0 & Q\end{pmatrix}, \quad (27)$$

with components given by

$$\sigma = -\frac{e^2}{3\pi^2}\int_m^\infty d\varepsilon\,\frac{p^3}{\varepsilon}\frac{\partial f^0}{\partial\varepsilon}\tau = \sigma_0+\sigma_2, \quad (28)$$

$$\sigma_l = -\frac{e^2}{3\pi^2}\int_m^\infty d\varepsilon\,\frac{p^3}{\varepsilon}\frac{\partial f^0}{\partial\varepsilon}\frac{\tau(\omega_c\tau)^l}{1+(\omega_c\tau)^2}, \quad (29)$$

$$\alpha = \frac{e}{3\pi^2}\int_m^\infty d\varepsilon\,\frac{p^3}{\varepsilon}\frac{\partial f^0}{\partial\varepsilon}\left(\frac{\varepsilon-\mu}{T}\right)\tau = \alpha_0+\alpha_2, \quad (30)$$

$$\alpha_l = \frac{e}{3\pi^2}\int_m^\infty d\varepsilon\,\frac{p^3}{\varepsilon}\frac{\partial f^0}{\partial\varepsilon}\left(\frac{\varepsilon-\mu}{T}\right)\frac{\tau(\omega_c\tau)^l}{1+(\omega_c\tau)^2}, \quad (31)$$

$$\tilde{\kappa} = -\frac{T}{3\pi^2}\int_m^\infty d\varepsilon\,\frac{p^3}{\varepsilon}\frac{\partial f^0}{\partial\varepsilon}\left(\frac{\varepsilon-\mu}{T}\right)^2\tau = \tilde{\kappa}_0+\tilde{\kappa}_2, \quad (32)$$

$$\tilde{\kappa}_l = -\frac{T}{3\pi^2}\int_m^\infty d\varepsilon\,\frac{p^3}{\varepsilon}\frac{\partial f^0}{\partial\varepsilon}\left(\frac{\varepsilon-\mu}{T}\right)^2\frac{\tau(\omega_c\tau)^l}{1+(\omega_c\tau)^2}, \quad (33)$$

which allows us to write down the components of the thermopower

$$Q = -\frac{\alpha}{\sigma}, \qquad Q_0 = -\frac{\alpha_0\sigma_0+\alpha_1\sigma_1}{\sigma_0^2+\sigma_1^2}, \qquad Q_1 = -\frac{\alpha_1\sigma_0-\alpha_0\sigma_1}{\sigma_0^2+\sigma_1^2}. \quad (34)$$

Our numerical computations below concentrate on the thermal conductivity given by the matrix

$$\hat{\kappa} = \begin{pmatrix} \kappa_0 & -\kappa_1 & 0 \\ \kappa_1 & \kappa_0 & 0 \\ 0 & 0 & \kappa \end{pmatrix}, \tag{35}$$

where the coefficients are defined as

$$\kappa = \tilde{\kappa} + T\alpha Q = \tilde{\kappa} - T\frac{\alpha^2}{\sigma}, \tag{36}$$

$$\kappa_0 = \tilde{\kappa}_0 + T(\alpha_0 Q_0 - \alpha_1 Q_1), \tag{37}$$

$$\kappa_1 = \tilde{\kappa}_1 + T(\alpha_0 Q_1 + \alpha_1 Q_0), \tag{38}$$

where κ is the longitudinal, κ_0 is the transverse, and κ_1 is the Hall component of the thermal conductivity. Note that the components of the thermal conductivity tensor are fully determined if the relaxation time τ is known. We evaluate the scattering matrix of electrons by ions using the standard QFT methods. The many-body correlations are taken into account through the structure-function of ions determined from Monte Carlo simulations of one-component plasma and screening of ionic charge in the hard-thermal loop approximation given by Equation (17). We also take into account the finite size of ions by multiplying the matrix element with a suitable function of the radius of the nucleus (see Ref. [13,29] for details). Finally, we cast Equation (26) in the following form:

$$\boldsymbol{E}' = \varrho \boldsymbol{j}_{\parallel} + \varrho_0 \boldsymbol{j}_{\perp} + R[\boldsymbol{B} \times \boldsymbol{j}] - Q\nabla_{\parallel} T - Q_0 \nabla_{\perp} T + N[\boldsymbol{B} \times \nabla T], \tag{39}$$

$$\boldsymbol{q} = -\kappa \nabla_{\parallel} T - \kappa_0 \nabla_{\perp} T + L[\boldsymbol{B} \times \nabla T] - TQ\boldsymbol{j}_{\parallel} - TQ_0 \boldsymbol{j}_{\perp} + D[\boldsymbol{B} \times \boldsymbol{j}], \tag{40}$$

where $\parallel$ and $\perp$ denote the components of vectors that are parallel and perpendicular to the magnetic field with

$$\varrho = \frac{1}{\sigma}, \qquad \varrho_0 = \frac{\sigma_0}{\sigma_0^2 + \sigma_1^2}, \qquad \varrho_1 = \frac{\sigma_1}{\sigma_0^2 + \sigma_1^2}, \tag{41}$$

denoting the components of the electrical resistivity tensor $\hat{\varrho} = \hat{\sigma}^{-1}$.

Here, we introduced the Hall coefficient $R = -\rho_1/B$, the Nernst coefficient $N = -Q_1/B$, the Righi–Leduc coefficient $L = -\kappa_1/B$, and the Ettingshausen coefficient $D = -TQ_1/B = NT$. The physical content of each term is easily read off from the corresponding terms in the currents (39) and (40). Below, we focus on the thermal conductivity and the thermal Hall effect, which describes the heat flow orthogonal to the temperature gradient under an imposed magnetic field. Its efficiency is measured by the Righi–Leduc coefficient L. Clearly, it is an analog of the electrical Hall effect ($\propto R$ in Equation (39)), which occurs when a magnetic field is applied perpendicular to an electric current in a conductor, causing the charge carriers (electrons) to create a voltage across the system.

5. Results

In this section, we focus on our results for thermal conductivity and thermal Hall effect. Numerically, these are evaluated using the relaxation time Equation (16) and the formulas in Equations (28)–(34), and (36)–(38). We recall that in large magnetic fields ($\omega_c\tau \gtrsim 1$) the tensor structure of these quantities becomes important, while for low magnetic fields ($\omega_c\tau \to 0$) only the longitudinal thermal conductivity κ is relevant. In the isotropic case $\omega_c\tau \ll 1$, one has $\sigma_1 \ll \sigma_0 \simeq \sigma$; therefore, all three diagonal components of the conductivity tensor are identical, and the non-diagonal components vanish. In the anisotropic case $\omega_c\tau \simeq 1$, they are distinct and should be studied separately. Below, we will study the dependence of the conductivity on the density, temperature, and strength of the magnetic field for the selected compositions.

5.1. Results for Relaxation Times

Figure 2 provides numerical values of the relaxation time as a function of temperature. As discussed above, τ depends on the electron energy; therefore it is evaluated at the Fermi

energy in the degenerate regime (left panels) and at the thermal energy $\bar{\varepsilon} = 3T$ in the nondegenerate (right panels) regime. Our results agree well with those of Nandkumar and Pethick [7] in the degenerate regime, which are shown on our plots with circles. The values of their I_1 integral were read-off from the solid lines shown in Figures 2 and 3, which correspond to screening in the random-phase-approximation including vertex corrections. These were then used with Equation (9) to compute the relaxation time. It is seen that τ decreases as a function of temperature in the degenerate regime and increases in the nondegenerate regime. The decrease in the relaxation time with the temperature in the degenerate regime is caused practically by the structure factor $S(q)$. For comparison we evaluated also the relaxation time without taking into account the structure factor in Figure 2. In the nondegenerate regime, the temperature dependence of τ is dominated by the energy increase in electrons with temperature, and the role of $S(q)$ is less important, especially for light nuclei. This is due to the fact that when $T \geq T_F$, i.e., electrons are nondegenerate, the ionic component forms a weakly coupled Boltzmann gas (see Figure 1).

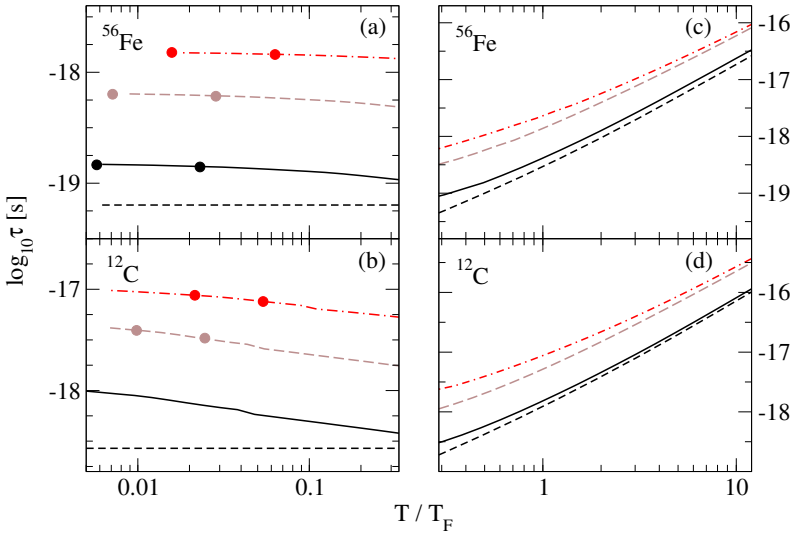

Figure 2. The relaxation time as a function of dimensionless ratio T/T_F for three values of density: $\log_{10}\rho = 10$ (solid lines), $\log_{10}\rho = 8$ (dashed lines), and $\log_{10}\rho = 6$ (dash-dotted lines) for ^{56}Fe [(**a**,**c**)] and ^{12}C [(**b**,**d**)]. Panels (**a**,**b**) correspond to the degenerate regime, and (**c**,**d**) to the nondegenerate regime. To demonstrate the effect of ion–ion correlations, we show the results for $\log_{10}\rho = 10$ in the case where $S(q) = 1$ by short-dashed lines. The circles reproduce the results of Ref. [7].

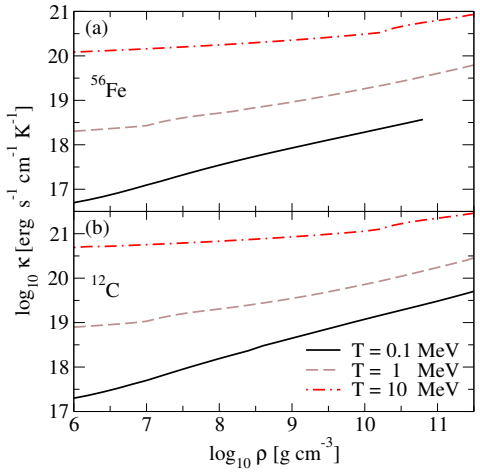

Figure 3. Dependence of the longitudinal conductivity on density for various values of temperature for (**a**) ^{56}Fe; (**b**) ^{12}C.

5.2. Longitudinal Thermal Conductivity

We start the discussion of our numerical results with the density, temperature, and composition dependence of the longitudinal thermal conductivity κ. Figure 3 shows the thermal conductivity as a function of density for various temperatures for the crustal matter consisting of ^{56}Fe and ^{12}C nuclei. The chosen values of the temperature cover both the non-degenerate ($T = 10$ MeV) and the degenerate ($T = 0.1$ MeV) regimes for electrons with the value $T = 1$ MeV being representative for transition between these two regimes (the transition density is around $\log_{10} \rho \simeq 7.5$ g cm^{-3} for both types of nuclei, see Figure 1). The thermal conductivity shows a power-law increase in density $\kappa \propto \rho^{\alpha}$ with $\alpha_{Fe} \simeq 0.37$ and $\alpha_C \simeq 0.43$ in the degenerate regime, and $\alpha \simeq 0.08$ (for both nuclei) in the non-degenerate regime. This behavior is similar to the density-dependence of the electrical conductivity, which is a consequence of different density and temperature dependence of the relaxation time in these regimes (see Ref. [13] for details).

The main difference between the values of κ for different nuclei arise from the scaling $\kappa \sim n_e \tau \sim Z n_i \tau \sim (Z/A)\tau \simeq 0.5\tau$, $\tau^{-1} \sim Z^2 n_i \sim Z^2/A \simeq 0.5Z$, as seen from Equation (16), therefore $\kappa \sim Z^{-1}$. Thus, the expected ratio of two conductivities is $\kappa_C/\kappa_{Fe} \simeq 4.3$ (in the nondegenerate limit) , which are consistent with the results shown in Figure 3.

The temperature dependence of the thermal conductivity is shown in Figure 4. The dotted lines show the low- and high-temperature asymptotics. The scaling of κ with the temperature is $\kappa \propto T^{\gamma}$ with $\gamma_{Fe} \simeq 0.95$, $\gamma_C \simeq 0.8$ in the degenerate and $\gamma \simeq 1.8$ in the non-degenerate regime. In the degenerate regime, the temperature dependence of κ (or τ) is stronger for lighter elements, because at any given density and temperature, the parameter Γ is smaller for lighter elements ($\Gamma \sim Z^2/A^{1/3}$, e.g., $\Gamma_{Fe}/\Gamma_C \simeq 11$), and the structure factor $S(q)$ varies faster for small values of Γ, assuming that $a_i q$ is small.

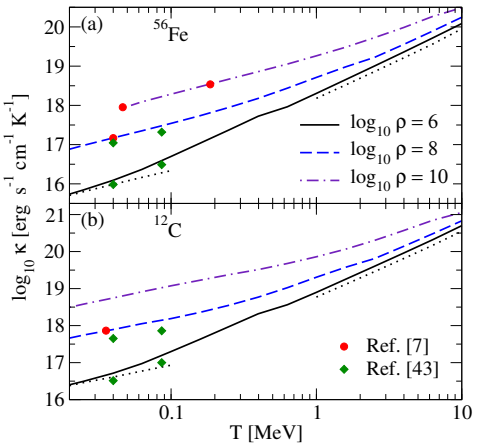

Figure 4. The temperature dependence of the thermal conductivity for three values of density for ^{56}Fe (**a**) and ^{12}C (**b**). The dots represent the low- and high-temperature asymptotics. The red circles show the results of Ref. [7] obtained from their values of I_1 integrals given by solid lines in Figures 2 and 3 and Equation (15). The green diamonds show the results listed in the table of Ref. [43].

For the sake of comparison, we show in Figure 4 the low-temperature results of Ref. [7], which are in very good agreement with ours. Note that both computations take into account the electron–ion collisions but neglect the electron–electron ones. They also use fits to the same data for the static structure factor $S(q)$. However, they treat the screening effects encoded in the electron polarization tensor differently: Ref. [7] uses the highly degenerate limit of the random-phase-approximation of the polarization tensor including vertex corrections in the static limit; our study utilizes the hard-thermal-loop approximation to the dynamical polarization tensor (see Ref. [13] and references therein). We also show the results extracted from the table provided by Ref. [43] for $T = 8.64 \cdot 10^8$ K and $T = 10^9$ K, the largest value for temperature available. Our values of κ are larger by about 30–40% for ^{56}Fe and 50–75% for ^{12}C compared to this work. The main difference is that Ref. [43]

includes electron–electron collisions in addition to electron–ion collisions. The structure factor used in this work differs from ours: it utilizes the fits of Ref. [37] to hypernetted chain computations for one-component plasma, whereas we use data based on older Monte Carlo simulations of liquid structure function for the same system [38–40]. Similarly to the previous case, the treatments of the electron polarization tensor are not identical in terms of approximation and inclusion of dynamical effects.

5.3. Transverse and Hall Conductivities

The transverse (κ_0) and Hall (κ_1) components of the thermal conductivity depend on the value of the Hall parameter $\omega_c\tau$, which for homogeneous magnetic fields decreases with the density because of the decrease in relaxation time in any regime as well as because of the decrease in ω_c in the degenerate regime. Thus, at low densities, the crust becomes more anisotropic, and for $\omega_c\tau \gg 1$ we have

$$\kappa_0 \simeq \frac{\kappa}{(\omega_c\tau)^2} \simeq \left(\frac{\pi^2 n_e T}{3eB}\right)^2 \kappa^{-1} \ll \kappa. \tag{42}$$

Because $\omega_c\tau$ decreases with the density, the component κ_0 increases with density faster than κ according to scaling $\kappa_0 \propto \rho^\beta$, $\beta \simeq 1.6$ in the degenerate regime, and $\beta \simeq 1.85$ in the nondegenerate regime, and tends to κ_0 in the high-density regime (see Figure 5). The scaling of κ_0 with respect to Z is the inverse of κ, i.e., $\kappa_0 \sim \tau^{-1} \sim Z$. Thus, κ_0 is smaller for lighter elements in the strongly anisotropic regime. We see from Equation (42) that for a given density $\kappa_0/T \sim (\kappa/T)^{-1}$, therefore κ_0/T shows an inverted temperature dependence at low densities.

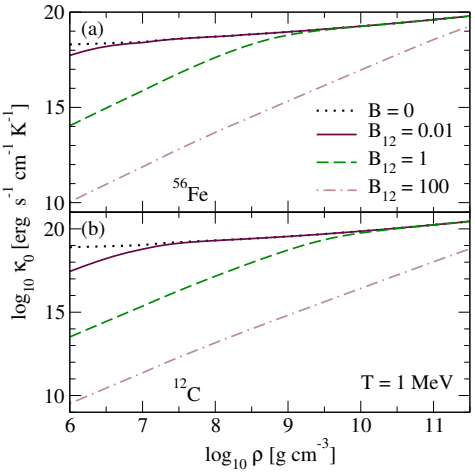

Figure 5. Dependence of the transverse component of the thermal conductivity tensor on density for various values of the B-field for (**a**) ^{56}Fe; (**b**) ^{12}C. The temperature is fixed at $T = 1$ MeV. The dotted lines show the limit of vanishing magnetic field, i.e., the longitudinal conductivity.

For the Hall component, we find the following limiting expressions

$$\kappa_1 \simeq (\omega_c\tau)\kappa \simeq \frac{3e}{\pi^2}\frac{B}{n_e T}\kappa^2, \qquad \omega_c\tau \ll 1, \tag{43}$$

$$\kappa_1 \simeq \frac{\kappa}{\omega_c\tau} \simeq \frac{\pi^2}{3e}\frac{n_e T}{B}, \qquad \omega_c\tau \gg 1. \tag{44}$$

At low densities and/or large magnetic fields $\omega_c\tau \gg 1$, and κ_1 increases linearly with the density and temperature, but does not depend on the type of nuclei. At high densities, κ_1 decreases slowly with the density, as implied by Equation (43) (see Figure 6). At the point where $\omega_c\tau \simeq 1$, the transition between these two regimes occurs, and κ_1 displays a maximum there.

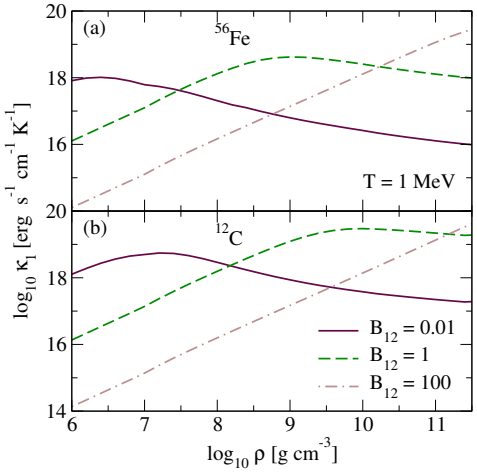

Figure 6. Dependence of the Hall component of the thermal conductivity tensor on density for various values of the B-field for (**a**) ^{56}Fe; (**b**) ^{12}C. The temperature is fixed at $T = 1$ MeV.

In the isotropic region we have also $\kappa_1/T \propto (\kappa/T)^2$ and $\kappa_1 \propto Z^{-2}$ for $Z > 1$, therefore κ_1 is larger for ^{12}C by an order of magnitude as compared to ^{56}Fe. As τ is larger for light elements, the anisotropic region for lighter elements is larger, and the maximum of κ_1 is shifted to higher densities. Correspondingly, the maximum value of κ is also larger for lighter elements.

Figures 7 and 8 show the dependence of κ_0 and κ_1 on the magnetic field. For low magnetic fields $\omega_c\tau \ll 1$, therefore $\kappa_0 \simeq \kappa$ and it does not depend on the value of the field. However, for $\omega_c\tau \gtrsim 1$ κ_0 it starts decreasing as $\kappa_0 \propto B^{-2}$. The scaling of the Hall conductivity on the magnetic field in the low-field and high-field limits is given by $\kappa_1 \propto B$ and $\kappa_1 \sim B^{-1}$, respectively, and the maximum is located around $\omega_c\tau \simeq 1$. The point of the maximum shifts to lower magnetic fields with the decrease in density and nucleus charge number. For $B_{12} = 1$, the crust is anisotropic at densities $\rho \leq 10^9$ g cm^{-3} for ^{56}Fe and at $\rho \leq 10^{10}$ g cm^{-3} for ^{12}C. For magnetic fields $B_{12} \geq 10$, the outer crust is almost entirely anisotropic for all nuclei.

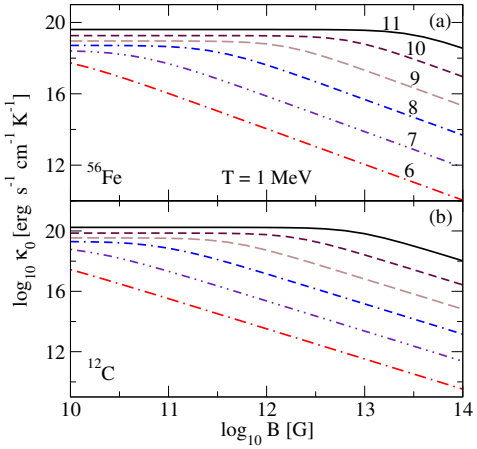

Figure 7. Dependence of κ_0 on the magnetic field for (**a**) ^{56}Fe; (**b**) ^{12}C for various values of $\log_{10}\rho/[\text{g cm}^{-3}]$ as indicated in the plots. The temperature is fixed at $T = 1$ MeV.

Finally, we show the modulus of the Righi–Leduc coefficient $L = \kappa_1/B$ as defined after Equation (41) in Figures 9 and 10, which has a negative sign for electrons. This coefficient is responsible for the thermal Hall effect, which might affect the thermal evolution of the star if large thermal gradients are present perpendicular to the magnetic field lines and the Hall parameter is close to unity $\omega_c\tau \simeq 1$, where $L \simeq \kappa/2B$. From Equations (43) and (44), we obtain for the limiting cases

$$L \simeq \frac{3e\kappa^2}{\pi^2 n_e T}, \qquad \omega_c\tau \ll 1, \tag{45}$$

$$L \simeq \frac{\pi^2}{3e}\frac{n_e T}{B^2}, \qquad \omega_c\tau \gg 1. \tag{46}$$

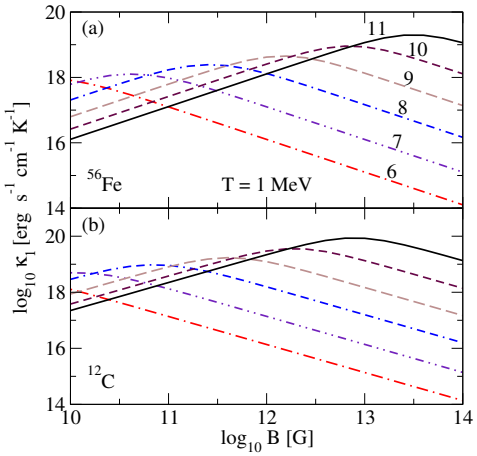

Figure 8. Dependence of κ_1 on the magnetic field for (a) ^{56}Fe; (**b**) ^{12}C for various values of $\log_{10}\rho/[\mathrm{g\ cm^{-3}}]$ as indicated in the plots. The temperature is fixed at $T = 1$ MeV.

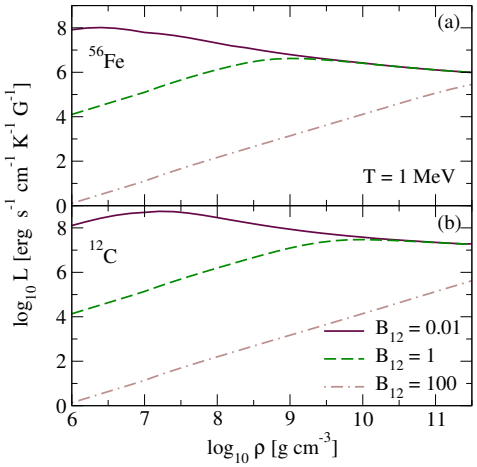

Figure 9. The modulus of the Righi–Leduc coefficient as a function of density for various values of the B-field for (**a**) ^{56}Fe; (**b**) ^{12}C. The temperature is fixed at $T = 1$ MeV.

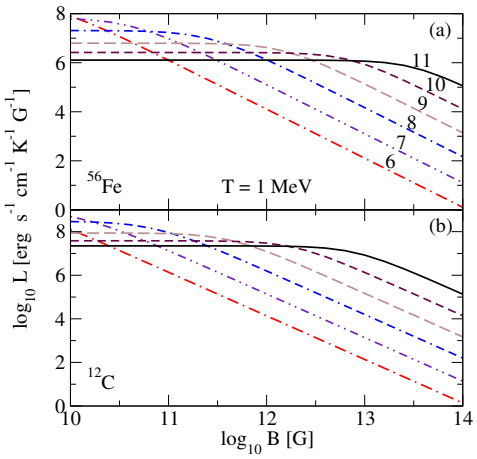

Figure 10. The modulus of the Righi–Leduc coefficient as a function of magnetic field for (**a**) ^{56}Fe; (**b**) ^{12}C for various values of $\log_{10}\rho/[\mathrm{g\ cm^{-3}}]$ as indicated in the plots. The temperature is fixed at $T = 1$ MeV.

5.4. Fits to the Conductivities

We have performed fits to the (longitudinal) electrical and thermal conductivities using the formulae

$$\sigma_{\rm fit} = \frac{1.5\times10^{22}}{Z}\left(\frac{T_F}{1\ {\rm MeV}}\right)^{a}\left(\frac{T}{T_F}\right)^{-b}\left(\frac{T}{T_F}+d\right)^{c}\ {\rm s}^{-1}. \quad (47)$$

$$\kappa_{\rm fit} = \frac{6\times10^{19}}{Z}\left(\frac{T}{1\ {\rm MeV}}\right)\left(\frac{\varepsilon_F}{T_F}\right)^{0.16}\left(\frac{T_F}{1\ {\rm MeV}}\right)^{a'}\left(\frac{T}{T_F}\right)^{-b'}\left(\frac{T}{T_F}+d'\right)^{c'}\ {\rm erg\ s^{-1}\ cm^{-1}\ K^{-1}}. \quad (48)$$

The fit parameters in Formula (47) depend on the charge (proton number) of the nucleus via the following formula:

$$a(Z) = 0.924 - 0.009\log Z + 0.003\log^2 Z, \quad (49)$$

$$b(Z) = 0.507 - 0.028\log Z - 0.025\log^2 Z, \quad (50)$$

$$c(Z) = 1.295 - 0.018\log Z - 0.022\log^2 Z, \quad (51)$$

$$d(Z) = 0.279 + 0.056\log Z + 0.035\log^2 Z. \quad (52)$$

The fit parameters in Formula (48) are given by

$$a'(Z) = 0.974 + 0.002\log Z + 0.003\log^2 Z, \quad (53)$$

$$b'(Z) = 0.393 - 0.009\log Z - 0.030\log^2 Z, \quad (54)$$

$$c'(Z) = 1.112 + 0.001\log Z - 0.025\log^2 Z, \quad (55)$$

$$d'(Z) = 0.224 + 0.028\log Z + 0.042\log^2 Z. \quad (56)$$

The relative error of the fit Formulas (47) and (48) is 10% in the temperature range 0.4 MeV $\leq T \leq$ 10 MeV. The density dependence in these formulas is by means of the electron Fermi temperature, which in general has the form $T_F = 0.511\left[\sqrt{1+(Z\rho_6/A)^{2/3}}-1\right]$ MeV with $\rho_6 = \rho/(10^6\,{\rm g\,cm^{-3}})$. For ultrarelativistic electrons, this simplifies to $T_F = 0.511(Z\rho_6/A)^{1/3} \simeq 0.4\rho_6^{1/3}$ MeV, where the second relation is valid for $Z/A \simeq 0.5$. Substituting this into Equations (47) and (48), we obtain fit formulas with explicit dependence on density (ultrarelativistic electrons)

$$\sigma_{\rm fit} \simeq CZ^{-1}\rho_6^{(a+b)/3}T_1^{-b}\left(T_1\rho_6^{-1/3}+yd\right)^{c}\ {\rm s}^{-1}, \quad (57)$$

$$\kappa_{\rm fit} \simeq C'Z^{-1}\rho_6^{(a'+b')/3}T_1^{1-b'}\left(T_1\rho_6^{-1/3}+yd'\right)^{c'}\ {\rm erg\ s^{-1}\ cm^{-1}\ K^{-1}}, \quad (58)$$

with $T_1 \equiv T/(1\ {\rm MeV})$, $C = 1.5\times10^{22}\times y^{a+b-c}$, $C' = 6\times10^{19}\times y^{a+b-c}$, and $y = 0.4$.

The average relaxation time τ and the Hall parameter $x \equiv \omega_c\tau$ can be fitted by the approximate formula

$$\tau_{\rm fit} = 1.94\times10^{-16}\times\frac{A}{Z^2\rho_6}\left(\frac{T_F}{1\ {\rm MeV}}\right)^{a}\left(\frac{T}{T_F}\right)^{-b}\left(\frac{T}{T_F}+d\right)^{c} \times\left[\varepsilon_{F1}\left(1+\frac{T}{T_F}\right)^{-1}+3T_1\left(1+\frac{T_F}{T}\right)^{-1}\right]{\rm s}, \quad (59)$$

$$x = 1.74\times10^{3}\times\frac{A}{Z^2}\frac{B_{12}}{\rho_6}\left(\frac{T_F}{1\ {\rm MeV}}\right)^{a}\left(\frac{T}{T_F}\right)^{-b}\left(\frac{T}{T_F}+d\right)^{c}, \quad (60)$$

where $\varepsilon_{F1} \equiv \varepsilon_F/(1\ {\rm MeV})$.

For the transverse and Hall components of conductivities, the following formulas can be used

$$\sigma_0^{\rm fit} = \frac{\nu\sigma_{\rm fit}}{1+(\nu x)^2}, \qquad \sigma_1^{\rm fit} = \frac{x\sigma_{\rm fit}}{1+x^2}, \tag{61}$$

$$\kappa_0^{\rm fit} = \frac{\nu\kappa_{\rm fit}}{1+(\nu x)^2}, \qquad \kappa_1^{\rm fit} = \frac{x\kappa_{\rm fit}}{1+x^2}, \tag{62}$$

where $\nu = (T_F/\varepsilon_F)^{0.16}$. The relative error of Formulas (61) and (62) is 15% and 20%, respectively.

6. Conclusions

Motivated by the potential importance of the transport phenomena in modeling the behaviour of finite-temperature electron-ion plasma in hot neutron stars, white dwarfs, and binary neutron star mergers, we have calculated the thermal conductivity and thermal Hall effect in such plasma at densities corresponding to the outer crusts of neutron stars and the interiors of white dwarfs, at temperatures from the melting temperature of the solid $\sim 10^9$ K up to 10^{11} K (10 MeV). This temperature range is relevant to the liquid state of electron-ion plasma and covers the transition from degenerate to non-degenerate regimes for electrons. In this regime, electron transport dominates, with electrons scattering off correlated nuclei via screened electromagnetic forces. The plasma correlations in the liquid state are accounted for using the ion structure-function derived from Monte Carlo simulation data of one-component plasma. We have incorporated hard-thermal-loop quantum electrodynamics polarization susceptibilities in the low-frequency limit, combined with a nonzero-temperature Debye screening length, which serves as a good approximation in scenarios where inelastic processes are suppressed by the large mass of nuclei. The Boltzmann kinetic equation is solved using the relaxation time approximation.

Our study of the thermal conductivity of crustal matter focused on ^{56}Fe and ^{12}C nuclei. The conductivity shows a power-law increase in density $\kappa \propto \rho^{\alpha}$ in both regimes of degenerate (with $\alpha \simeq 0.4$) and non-degenerate electrons (with $\alpha \simeq 0.08$), similar to the density-dependence of the electrical conductivity studied in Ref. [13].

The scaling of κ with the temperature is $\kappa \propto T^{\gamma}$ with $\gamma \simeq 0.9$ in the degenerate and $\gamma \simeq 1.8$ in the non-degenerate regime. We show also that the behavior of the ratio κ/T is rather similar to that of the electrical conductivity. Specifically, κ/T has a minimum which lies in the range of temperatures $0.1\,T_F \leq T \leq 0.15\,T_F$. The occurrence of the minimum is observed across the entire density range we considered. This phenomenon is linked to the expansion of phase space caused by rising temperature, which is effective at any given fixed density. Our results show good agreement with those of [7] for the relaxation time and the thermal conductivity in the low-temperature regime, where a comparison is possible (see Figures 2 and 4). There are, however, some differences in the input physics, notably the use of different approximation for the electron polarization tensor in Ref. [7]. Additionally, we compared our thermal conductivity calculations with the tabulated results in [43]. As explained already in Section 5.2, we find larger values of κ by about 30–40% for ^{56}Fe and 50–75% for ^{12}C nuclei (see Figure 3), mainly because our neglect of the electron–electron collisions. Additionally, both the static structure functions for one-component plasma and the electron polarization tensors have different origins (see Section 5.2), which might account for any potential differences.

We studied also the transverse (κ_0) and the Hall (κ_1) components of the thermal conductivity, as well as the Righi–Leduc coefficient $L = \kappa_1/B$ for nonquantizing magnetic fields $B \leq 10^{14}$ G. These components depend on the value of the Hall parameter $\omega_c\tau$, which decreases with density. As a result, the low-density regions of the crust are more anisotropic, meaning that the thermal conduction is suppressed in the directions transverse to the magnetic field. This anisotropy sets in at the density where $\omega_c\tau \simeq 1$. In the high-field limit, we find the following scalings of the transverse $\kappa_0 \propto B^{-2}$ and Hall $\kappa_1 \sim B^{-1}$ conductivities on the magnetic field B. Our numerical results can be implemented in hydrodynamics simulations of warm compact stars also by means of accurate fit formulas. Large-scale simulations of the early phases of hot proto-neutron stars and post-merger remnants can shed light on the role of thermal conductivity and thermal Hall effect on the

turbulent fluid dynamics of these objects under the combined influence of strong magnetic fields and thermal gradients, potentially uncovering complex feedback loops between various factors.

While we focused here on thermal conductivity and the thermal Hall effect, we anticipate that the thermopower could play an equally important role in the dissipative dynamics of astrophysical electron-ion plasma in strong fields. We relegate the study of the thermopower as well as of the astrophysical implications of the present study to a future publication.

Author Contributions: The authors contributed equally to this work. All authors have read and agreed to the published version of the manuscript.

Funding: This research was funded by Deutsche Forschungsgemeinschaft grant number SE 1836/5-3, Polish National Science Centre (NCN) grant 2020/37/B/ST9/01937, Higher Education and Science Committee (HESC) of the Republic of Armenia Grant No. 24RL-1C010.

Data Availability Statement: The data underlying this article will be shared at a reasonable request by the corresponding author.

Acknowledgments: A.H. acknowledges the hospitality of Frankfurt Institute for Advanced Studies at Goethe University where part of this work was carried out.

Conflicts of Interest: The authors declare no conflicts of interest.

References

1. Flowers, E.; Itoh, N. Transport properties of dense matter. *Astrophys. J.* **1976**, *206*, 218–242. [CrossRef]
2. Yakovlev, D.G.; Urpin, V.A. Thermal and Electrical Conductivity in White Dwarfs and Neutron Stars. *Sov. Ast.* **1980**, *24*, 303.
3. Urpin, V.A.; Yakovlev, D.G. Thermogalvanomagnetic Effects in White Dwarfs and Neutron Stars. *Sov. Ast.* **1980**, *24*, 425.
4. Flowers, E.; Itoh, N. Transport properties of dense matter. III—Analytic formulae for thermal conductivity. *Astrophys. J.* **1981**, *250*, 750–752. [CrossRef]
5. Itoh, N.; Mitake, S.; Iyetomi, H.; Ichimaru, S. Electrical and thermal conductivities of dense matter in the liquid metal phase. I—High-temperature results. *Astrophys. J.* **1983**, *273*, 774–782. [CrossRef]
6. Itoh, N.; Kohyama, Y.; Matsumoto, N.; Seki, M. Electrical and Thermal Conductivities of Dense. *Astrophys. J.* **1984**, *285*, 758. [CrossRef]
7. Nandkumar, R.; Pethick, C.J. Transport coefficients of dense matter in the liquid metal regime. *Mon. Not. R. Astron. Soc.* **1984**, *209*, 511–524. [CrossRef]
8. Itoh, N.; Kohyama, Y. Electrical and Thermal Conductivities of Dense Matter in the Crystalline Lattice Phase. II. Impurity Scattering. *Astrophys. J.* **1993**, *404*, 268. [CrossRef]
9. Baiko, D.A.; Kaminker, A.D.; Potekhin, A.Y.; Yakovlev, D.G. Ion Structure Factors and Electron Transport in Dense Coulomb Plasmas. *Phys. Rev. Lett.* **1998**, *81*, 5556–5559. [CrossRef]
10. Potekhin, A.Y. Electron conduction in magnetized neutron star envelopes. *arXiv* **1999**, arXiv:9909100. [CrossRef]
11. Itoh, N.; Uchida, S.; Sakamoto, Y.; Kohyama, Y.; Nozawa, S. The Second Born Corrections to the Electrical and Thermal Conductivities of Dense Matter in the Liquid Metal Phase. *Astrophys. J.* **2008**, *677*, 495–502. [CrossRef]
12. Potekhin, A.Y.; Pons, J.A.; Page, D. Neutron Stars—Cooling and Transport. *Space Sci. Rev.* **2015**, *191*, 239–291. [CrossRef]
13. Harutyunyan, A.; Sedrakian, A. Electrical conductivity of a warm neutron star crust in magnetic fields. *Phys. Rev. C* **2016**, *94*, 025805. [CrossRef]
14. Harutyunyan, A.; Sedrakian, A. Electrical conductivity tensor of dense plasma in magnetic fields. *arXiv* **2016**, arXiv:1607.04541.
15. Alford, M.G.; Harris, S.P. Damping of density oscillations in neutrino-transparent nuclear matter. *Phys. Rev. C* **2019**, *100*, 035803. [CrossRef]
16. Alford, M.; Harutyunyan, A.; Sedrakian, A. Bulk Viscous Damping of Density Oscillations in Neutron Star Mergers. *Particles* **2020**, *3*, 34. [CrossRef]
17. Alford, M.; Harutyunyan, A.; Sedrakian, A. Bulk viscosity from Urca processes: n p e μ matter in the neutrino-trapped regime. *Phys. Rev. D* **2021**, *104*, 103027. [CrossRef]
18. Alford, M.; Harutyunyan, A.; Sedrakian, A. Bulk viscosity from Urca processes: n p e μ matter in the neutrino-transparent regime. *Phys. Rev. D* **2023**, *108*, 083019. [CrossRef]
19. Dolginov, A.Z.; Urpin, V.A. The Thermomagnetic Instability in Degenerate Cores of White Dwarfs. *Astrophys. Space Sci.* **1980**, *69*, 259–267. [CrossRef]
20. Blandford, R.D.; Applegate, J.H.; Hernquist, L. Thermal origin of neutron star magnetic fields. *Mon. Not. R. Astron. Soc.* **1983**, *204*, 1025–1048. [CrossRef]

21. Geppert, U.; Wiebicke, H.J. Amplification of neutron star magnetic fields by thermoelectric effects. I—General formalism. *Astron. Astrophys. Suppl. Ser.* **1991**, *87*, 217–228.
22. Wiebicke, H.J.; Geppert, U. Amplification of neutron star magnetic fields by thermoelectric effects. VI. Analytical approach. *Astron. Astrophys.* **1996**, *309*, 203–212.
23. Gakis, D.; Gourgouliatos, K.N. Revisiting thermoelectric effects in the crust of neutron stars. *arXiv* **2024**, arXiv:2402.14911. [CrossRef]
24. Kaminker, A.D.; Yakovlev, D.G.; Potekhin, A.Y.; Shibazaki, N.; Shternin, P.S.; Gnedin, O.Y. Magnetars as cooling neutron stars with internal heating. *Mon. Not. R. Astron. Soc.* **2006**, *371*, 477–483. [CrossRef]
25. Geppert, U. Magneto-Thermal Evolution of Neutron Stars with Emphasis to Radio Pulsars. *J. Astrophys. Astron.* **2017**, *38*, 46. [CrossRef]
26. Dehman, C.; Viganò, D.; Pons, J.A.; Rea, N. 3D code for MAgneto-Thermal evolution in Isolated Neutron Stars, MATINS: The magnetic field formalism. *Mon. Not. R. Astron. Soc.* **2023**, *518*, 1222–1242. [CrossRef]
27. Ascenzi, S.; Viganò, D.; Dehman, C.; Pons, J.A.; Rea, N.; Perna, R. 3D code for MAgneto-Thermal evolution in Isolated Neutron Stars, MATINS: Thermal evolution and light curves. *Mon. Not. R. Astron. Soc.* **2024**, *533*, 201–224. [CrossRef]
28. Harutyunyan, A.; Nathanail, A.; Rezzolla, L.; Sedrakian, A. Electrical resistivity and Hall effect in binary neutron star mergers. *Eur. Phys. J.* **2018**, *54*, 191. [CrossRef]
29. Harutyunyan, A.; Sedrakian, A.; Gevorgyan, N.T.; Hayrapetyan, M.V. Electrical conductivity of a warm neutron star crust in magnetic fields: Neutron-drip regime. *Phys. Rev. C* **2024**, *109*, 055804. [CrossRef]
30. Sedrakian, D.M.; Avetisian, A.K. Magnetohydrodynamics of plasma in the crust of a neutron star. *Astrofizika* **1987**, *26*, 489–500. [CrossRef]
31. Shternin, P.S.; Yakovlev, D.G. Electron thermal conductivity owing to collisions between degenerate electrons. *Phys. Rev. D* **2006**, *74*, 043004. [CrossRef]
32. Cassisi, S.; Potekhin, A.Y.; Pietrinferni, A.; Catelan, M.; Salaris, M. Updated Electron-Conduction Opacities: The Impact on Low-Mass Stellar Models. *Astrophys. J. Suppl.* **2007**, *661*, 1094–1104. [CrossRef]
33. Cassisi, S.; Potekhin, A.Y.; Salaris, M.; Pietrinferni, A. Electron conduction opacities at the transition between moderate and strong degeneracy: Uncertainties and impacts on stellar models. *Astron. Astrophys.* **2021**, *654*, A149. [CrossRef]
34. Lee, T.D. Hydrogen Content and Energy-Productive Mechanism of White Dwarfs. *Astrophys. J. Suppl.* **1950**, *111*, 625. [CrossRef]
35. Hubbard, W.B.; Lampe, M. Thermal Conduction by Electrons in Stellar Matter. *Astrophys. J. Suppl.* **1969**, *18*, 297. [CrossRef]
36. Jancovici, B. On the relativistic degenerate electron gas. *Il Nuovo C.* **1962**, *25*, 428–455. [CrossRef]
37. Young, D.A.; Corey, E.M.; Dewitt, H.E. Analytic fit to the one-component-plasma structure factor. *Phys. Rev. A* **1991**, *44*, 6508–6512. [CrossRef]
38. Hansen, J.P. Statistical Mechanics of Dense Ionized Matter. I. Equilibrium Properties of the Classical One-Component Plasma. *Phys. Rev. A* **1973**, *8*, 3096–3109. [CrossRef]
39. Galam, S.; Hansen, J.P. Statistical mechanics of dense ionized matter. VI. Electron screening corrections to the thermodynamic properties of the one-component plasma. *Phys. Rev. A* **1976**, *14*, 816–832. [CrossRef]
40. Tamashiro, M.N.; Levin, Y.; Barbosa, M.C. The one-component plasma: A conceptual approach. *Phys. Stat. Mech. Its Appl.* **1999**, *268*, 24–49. [CrossRef]
41. Ziman, J.M. *Principles of the Theory of Solids*; Cambridge University Press: Cambridge, UK, 1979.
42. Hernquist, L. Relativistic electron transport in a quantizing magnetic field. *Astrophys. J. Suppl. Ser.* **1984**, *56*, 325–367. [CrossRef]
43. Potekhin, A. Electron Conductivity of Stellar Plasma: Version 2021. Available online: http://www.ioffe.ru/astro/conduct/ (accessed on 25 October 2024).